



Constructing Mo^{5+} sites in molybdenum oxide by lattice stress for efficient ammonia synthesis

Yuxi Ren^a, Hang Xiao^a, Ben Chong^a, Mengyang Xia^a, Song Kou^a, Aofei Xu^b, Jia Li^b, Jiantao Liu^b, Honghui Ou^{a,*}, Zhiwei Ren^b, Guidong Yang^{a,*}

^a XJTU-Oxford International Joint Laboratory for Catalysis, School of Chemical Engineering and Technology, Xi'an Jiaotong University, Xi'an, Shaanxi 710049, China

^b Department of Orthopedics, The First Affiliated Hospital of Xi'an Jiaotong University, Xi'an, Shaanxi 710049, China

ARTICLE INFO

Keywords:

Alkali metal intercalation

Two-dimensional material

MoO_3

Electrocatalytic nitrogen fixation

ABSTRACT

Molybdenum oxide (MoO_3) is a promising catalyst for electrocatalytic nitrogen reduction (eNRR). However, Mo sites with saturated coordination are not favorable to stable N_2 adsorption. Herein, we employed sodium ions as electron donors to interact with the interlayer atoms of MoO_3 , causing localized lattice stress on it and weakening the M-O bond, thus inducing the Mo^{5+} active sites (Na_xMoO_3). The N_2 temperature-programmed desorption (N_2 -TPD) result of the as-prepared Na_xMoO_3 exhibits that introducing Mo^{5+} could significantly improve the N_2 adsorption on the catalyst's surface. The optimized Na_xMoO_3 has an NH_3 yield of $41.3 \mu\text{g h}^{-1} \text{mg}^{-1}$ at ambient temperature and an FE of 21.4 %, which is in the relatively advanced position in the contemporaneous studies. Both experiments and density-functional theory (DFT) calculation demonstrated that the Mo^{5+} sites can effectively reduce the d-orbital energy level of Mo, which significantly enhances the interaction with N_2 .

1. Introduction

Ammonia (NH_3) is a kind of widely used chemical that promotes agriculture, the chemical industry, energy storage and other fields [1]. Nowadays, almost all NH_3 in industry is provided by the Haber-Bosch method, which requires huge energy input and brings heavy burdens on the global economy and ecological environment [2]. Therefore, it is of great significance to produce NH_3 under mild conditions. Recently, electrocatalytic nitrogen reduction reaction (eNRR) is considered as a promising approach to reduce fossil fuel consumption and carbon emissions [3]. However, extraordinarily high $\text{N}\equiv\text{N}$ bond energy (945 kJ mol^{-1}) and multiple competing reactions exert great pressure on NRR efficiency [4]. To achieve this goal, many scientists tentatively adopt laser, plasma and so on to pre-activate N_2 to improve the NH_3 yield rate [5–7]. Even so, the development of efficient NRR catalysts is still the destination for achieving mild NH_3 production [8,9]. It is necessary to develop efficient and durable NRR electrocatalysts.

As an effective component of nitrogenase, Mo adsorbs N_2 efficiently and attracts a lot of attention from scientists [10,11]. Recently, many published studies have demonstrated that Mo-based catalysts like MoS_2 , Mo_2C , Mo single atoms, Mo-based alloys, and so on have eNRR activity [12–15]. Compared to other Mo-based catalysts, MoO_3 has a relatively

inert hydrogen evolution performance and its surface sites' Lewis-strong acidity allows for more efficient N_2 fixation [16,17]. However, Mo sites with saturated coordination are not favorable to the stable presence of N_2 on its surface [18]. Some reports suggest that Mo sites with unsaturated coordination have better N_2 adsorption properties [19]. Recently, many scientists have utilized lattice defects in MoO_3 to alter the coordination environment of the central Mo atoms to enhance the catalytic activity. For example, Liu et al. designed 2D amorphous MoO_{3-x} to expose more Mo^{5+} sites to serve as electron trapping centers for π -backdonation of N_2 , which significantly enhances the NRR performance [20]. Xian et al. induced lattice defects in MoO_3 by doping iron and are beneficial for N_2 adsorption at the active sites [21]. Despite these breakthroughs, the currently reported strategies usually make the crystal structure more complex, which may fuel the hydrogen evolution reaction.

Inspired by the special two-dimensional structure, MoO_3 's van der Waals interlayers, which could be embedded in many small guest species, are a suitable space for modifying the coordination structure [22, 23]. Owing to the extremely active property and ultra-small size, alkali metal ions are often used as intercalation species to modify the physical, chemical, and electronic properties of two-dimensional materials [24]. Thus, we infer that the Mo sites with unsaturated oxygen coordination

* Corresponding authors.

E-mail addresses: ouhonghui@xjtu.edu.cn (H. Ou), guidongyang@xjtu.edu.cn (G. Yang).

<https://doi.org/10.1016/j.apcatb.2024.124066>

Received 15 January 2024; Received in revised form 28 March 2024; Accepted 9 April 2024

Available online 10 April 2024

0926-3373/© 2024 Elsevier B.V. All rights reserved.

can be precisely induced by alkali metal ions intercalation without excessive disruption of the bulk phase. As far as we are aware, exploring the effect of alkali metal ions modification on eNRR activity of two-dimensional materials has not been reported yet.

Herein, we report an alkali metal cation intercalation strategy to tune the electronic structure of MoO_3 to enhance its NRR activity. The sodium ions serve as the electron donor to interact with the interlayer oxygen atoms of MoO_3 . The XRD and TEM results show that the localized stresses were generated after the Na intercalation process and distorted the lattice structure of MoO_3 . The XPS results confirmed the generation of Mo^{5+} sites in the as-prepared Na_xMoO_3 . The electrochemical experiments demonstrate that the optimized Na_xMoO_3 -3 owns a rapid NH_3 yield rate of $41.3 \mu\text{g h}^{-1} \text{mg}^{-1}$ and an FE of 21.4 % at -1.2 V vs Ag/AgCl under ambient conditions, which was superior to that of the pristine MoO_3 . Density functional theories (DFT) calculations present that the d orbital of Na_xMoO_3 with Mo^{5+} sites matches with that of N_2 better, which is in favor of the d orbital electrons efficiently transfer to the N_2 's empty π^* orbital, thus activating the $\text{N}\equiv\text{N}$ bond. We also simulated the evolution of N_2 on the Na_xMoO_3 's surface, revealing the NRR mechanism. This work offers a new insight into designing novel eNRR catalysts.

2. Experimental section

2.1. Chemicals and materials

Sodium molybdate dihydrate ($\text{Na}_2\text{MoO}_4 \cdot 2 \text{H}_2\text{O}$, 99 %), hydrochloric acid (HCl), methanol (CH_3OH , 99 %), ethanol ($\text{C}_2\text{H}_6\text{O}$, 99 %), and sodium borohydride (NaBH_4 , 99 %) were purchased from Aladdin. Ultrapure water was obtained from a water purification system (OSJ-UP).

2.2. Synthesis of the MoO_3

In this synthesis, 2.4195 g of Sodium molybdate dihydrate and 3 mL of concentrated hydrochloric acid were added into 37 mL of ultrapure water with magnetically stirring for 30 min. The above solution was put into a Teflon-lined stainless steel autoclave and heated to 200°C for 12 h. After the autoclave cooled to room temperature, the supernatant was discarded and the residual product at the bottom of Teflon vessel was collected by centrifugation, rinsed with ultrapure water and ethanol for several times and dried at 60°C overnight. Finally, the obtained powder was annealing at 500°C for 2 h to remove all impurities.

2.3. Synthesis of the Na_xMoO_3

In this synthesis, 0.143 g of the prepared MoO_3 was dispersed in 10 mL of ethanol. And then, 1, 3, 5 mg/mL NaBH_4 ethanol solution was separately added into the mixture and magnetically stirred at room temperature for 2 h. The supernatant was discarded and the residual product was collected by centrifugation, rinsed with ultrapure water and ethanol for several times and freeze-drying overnight. The obtained samples separately named Na_xMoO_3 -1, Na_xMoO_3 -3, Na_xMoO_3 -5.

2.4. Characterization

Several instruments were used to characterize all the samples. The phase composition was determined by a powder X-ray diffractometer (XRD, Shimadzu 6100). The information of morphology and lattice diffraction was obtained by a scanning electron microscope (SEM, TE MAIA3 LMH) and a transmission electron microscope (TEM, Thermo Fisher Talos F200X). The UV spectrometer (Shimadzu 2600) was used to produce UV-vis diffuse reflectance spectra. Specific Na content was determined by inductively coupled plasma mass spectrometer (ICP, Perkin Elmer NexION 350D ICP-MS). A chemisorption device was used to acquire temperature-programmed desorption (TPD) data for the as-prepared materials (Quantachrome, Autosorb-iQC-TPX). The chemical

composition and valence state were determined by X-ray photoelectron spectroscopy (XPS, Thermo Fisher ESCALAB Xi+). The anode products were studied by attenuated total reflection fourier transform infrared spectrometer (ATR-FTIR, Nicolet iS50). And the intermediate species and productions of NRR were detected by time-resolved FT-IR Spectrometer (FTIR, Bruker INVENIO X).

2.5. Preparations of the working electrodes

Used as the support material, the carbon paper (CP) was first sonicated successively in acetone, water, and ethanol. Then, 6 mg of MoO_3 and Na_xMoO_3 and 50 μL of 5 wt% Nafion solution were dispersed in a mixture of 950 μL of ethanol. After sonication for 1 h, the MoO_3 and Na_xMoO_3 ink was obtained. Finally, 50 μL of the ink was dropped on the CP ($1 \times 1 \text{ cm}^{-2}$) and dried under ambient conditions, which was used as the working electrode for NRR measurements.

2.6. Electrochemical measurements

All electrochemical measurements were performed on an electrochemical workstation (Corrtest CS310X) in conventional three-electrode system using an H-type cell with Nafion membrane. Before the test, the Nafion 117 membrane was pretreated by boiling in H_2O_2 (5 %) solution, 0.5 M H_2SO_4 solution and DI water for 1 h at 80°C , successively. The prepared cathode, carbon rod, and Ag/AgCl were used as the working electrodes, counter electrodes and reference electrodes, respectively. To enhance the NRR efficiency, we prepared a 0.05 M LiCl solution using methanol as a solvent and added a small amount of water (volume fraction: 0.16 %) as a proton source. Both cathode cell and anode cell contained 30 mL as-prepared 0.05 M LiCl/methanol-water electrolyte. To remove the possible impurities, the feeding N_2 was purified through two acidic absorption cells (containing 1 M KOH solution and 0.5 M H_2SO_4 solution, respectively). And the cathode electrolyte was purged with N_2 for 30 min before every test and continuously fed at a gas flow rate of 10 mL min^{-1} during the experiments. For the blank experiments, N_2 was replaced with Ar, while the other conditions remained the same. The linear sweep voltammogram curves were recorded at a scan rate of 5 mV s^{-1} .

2.7. Determination of NH_3 and N_2H_4

The indophenol blue method was used to quantitatively determine the NH_3 content. The indicator solutions were prepared early and freshly: a 1 M NaOH solution containing 5 wt% sodium citrate and 5 wt % salicylic acid (solution A), 1 M NaOH solution containing 0.05 M NaClO (solution B), and a 1 wt% sodium nitroferrocyanide solution (solution C). Subsequently, the sample electrolyte (2 mL), solution A (2 mL), solution B (1 mL), and solution C (200 μL) were put into a colorimetric tube in sequence. After 2 h of reaction, the ultraviolet-visible (UV-vis) spectra of the resulting solution were measured at $\lambda = 655 \text{ nm}$. The standard curve was obtained by testing a standard NH_4^+ solution (0.0, 0.2, 0.4 and $1.0 \mu\text{g/mL}$ in ultrapure water). Additionally, all the measured absorbance was calibrated by the standard curve. The produced N_2H_4 in the cathodic reaction vessel was determined by the Watt and Chrisp method. Firstly, 5.99 g of PDAB and 30 mL of HCl were added into 300 mL of ethanol as the indicator reagent. Subsequently, the electrolyte (2 mL) was added into the colorimetric tube, after which the indicator reagent (2 mL) was added. After 15 min, the UV-vis spectra of the solution were recorded, and the final concentration was calibrated by the standard curve.

NH_3 yield rate was calculated using the following equation:

$$\text{NH}_3 \text{ yield rate} = [\text{NH}_4^+] \times V / (m \times t) \quad (1)$$

FE was calculated according to the following equation:

$$\text{FE} = 3 \times F \times [\text{NH}_4^+] \times V / (17 \times Q) \quad (2)$$

where $[\text{NH}_4^+]$ is the measured NH_4^+ ion concentration; V is the volume of the cathodic reaction electrolyte; t is the potential applied time; m is the loaded mass of catalyst; F is the Faraday constant; and Q is the total charge during tests.

2.8. Computational simulation details

Density functional theory calculation for NRR on the $\text{MoO}_3(110)$ and $\text{Na}_x\text{MoO}_3(110)$ is performed to on the Vienna ab initio simulation package (VASP). The Perdew-Burke-Ernzerhof (PBE) functional of the generalized gradient approximation (GGA) was adopted as the exchange-correlation functional.

3. Results and discussion

3.1. Synthesis and characterization

Na-intercalated MoO_3 nanobelts were successfully prepared by a two-step method (Fig. 1a). Briefly, ultrathin MoO_3 nanobelts were first obtained by a one-step hydrothermal synthesis between $\text{Na}_2\text{MoO}_4 \cdot 2\text{H}_2\text{O}$, HCl, and ultrapure water. Then, a solution reaction was employed to achieve the Na intercalation at room temperature. After two hours, the Na content in the samples was nearly unchanged, indicating that the reaction had been done (Figure S1). We characterized the composition of all samples. As shown in Fig. 1b and Figure S2, X-ray diffraction (XRD) results of both original and Na-intercalated samples are well indexed to MoO_3 (JCPDS No. 05-0508) [25]. The characteristic peaks at 12.76° , 25.70° , and 38.97° separately correspond to (020), (040), and (060) planes of MoO_3 . After Na intercalation, all the characteristic peaks shift to diffraction angles compared to the pristine MoO_3 . According to the Bragg formula ($2d\sin\theta=n\lambda$), the lattice spacing of these planes is expanded, exhibiting the stress effect inside the lattice after intercalation [26]. Based on the crystal structure of MoO_3 , the interlayer distance is obtained by calculating the spacing of interlayer

crystal planes (020) [27]. The final results are listed in Table S1, the interlayer spacing is changed from 6.923 \AA to 6.951 \AA , indicating the insertion of heteroatoms [28]. Meanwhile, the crystallinity of MoO_3 weakened with increasing Na content, suggesting that the lattice is distorted under interaction with intercalated Na ions. We employed X-ray photoelectron spectroscopy (XPS) to characterize the elemental composition and chemical states of MoO_3 and Na_xMoO_3 . According to the full spectrum of Na_xMoO_3 (Figure S3a), there is no obvious peak of B 1 s. It suggests that the residual ions on the surface of the Na_xMoO_3 have been completely removed. After intercalation, characteristic peaks of Mo^{6+} shifted to the lower binding energy, indicating the electrons acquired. A small amount of unsaturated Mo^{5+} sites emerged, located at 231.4 eV and 234.5 eV (Fig. 1c) [29]. A similar electron transfer phenomenon has also occurred in the lattice oxygen atoms (Figure S3b). Thus, considering the above XRD results, we conclude that Na ions, as electron donors, have interacted with interlayer oxygen atoms, finally distorting the lattice and influencing the local electronic structure of Mo sites [30]. In Fig. 1d, shows the high-resolution XPS spectrum of Na 1 s (1071.87 eV) in Na_xMoO_3 , which is not detected in the pristine MoO_3 [31]. Combined with the XRD results, this obtained results manifested that Na was successfully embedded into MoO_3 . To explore the interaction between Na and MoO_3 , the energy of Na located at different sites is calculated. There are two different kinds of interaction between Na and MoO_3 : interlayer intercalation and heteroatomic insertion. Because MoO_3 has two kinds of O that have different chemical states, we use subscript numbers to distinguish them (Figure S4). Compared to other situations (Na replaces Mo: unstable; Na replaces O1 and O2: -509.57 and -508.05 eV ; Na occupies interstitial position: unstable), the energy of interlayer intercalation is the lowest. That means Na is more likely to be inserted into the van der Waals interlayers to interact with MoO_3 and distort its lattice structure. The conclusion is consistent with the XRD results.

The scanning electron microscopy (SEM) image showed the as-prepared MoO_3 nanobelts with a width of about 200 nm (Figure S4a).

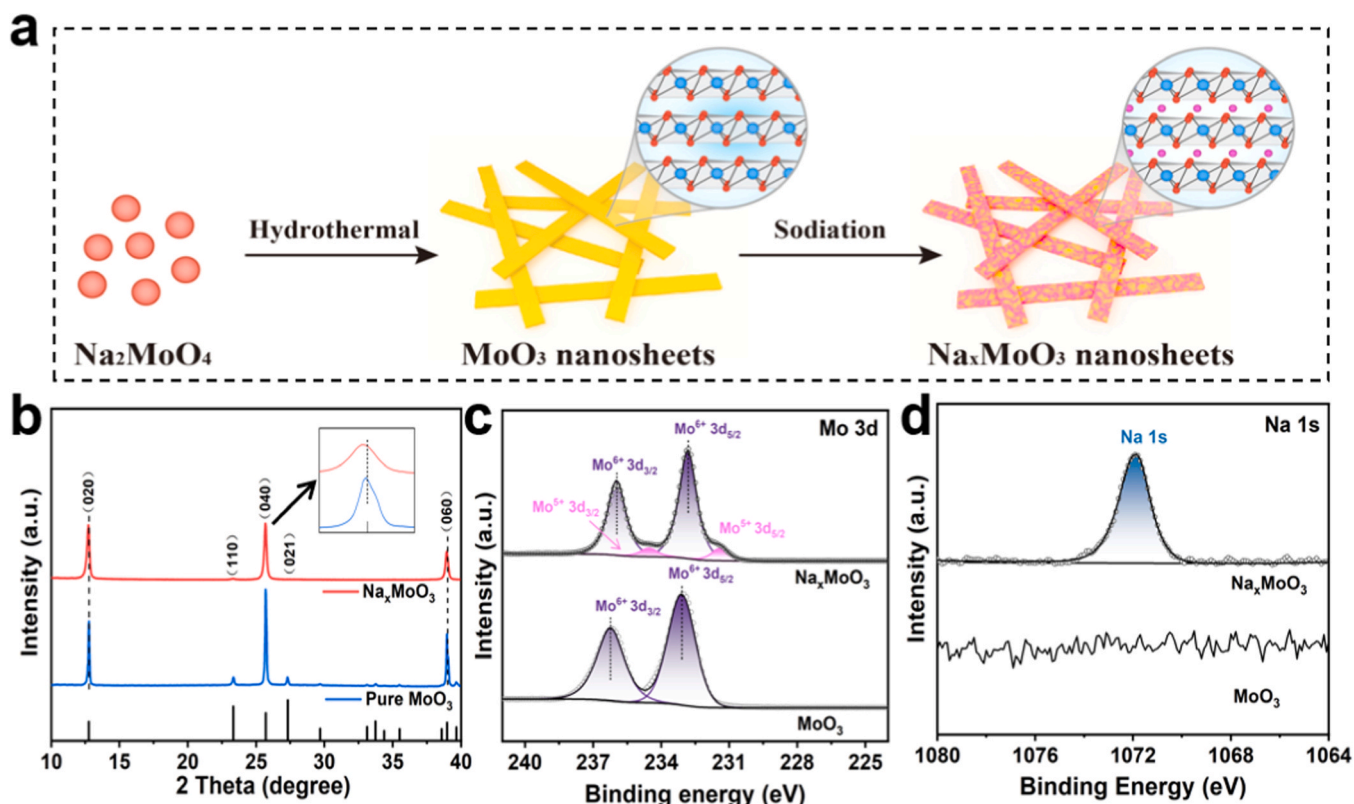


Fig. 1. (a) Synthetic scheme of Na_xMoO_3 . (b) XRD pattern of Na_xMoO_3 -3. XPS spectra of (c) Mo 3d and (d) Na 1s of Na_xMoO_3 -3.

After Na intercalation, there is no significant morphological change occurs in the Na_xMoO_3 compared to the pure MoO_3 (Figure S5b-d). The transmission electron microscopy (TEM) images of MoO_3 and Na_xMoO_3 -3 (Fig. 2a and b) further confirmed its ultrathin nanobelts structure. In the high-resolution TEM (HRTEM) pattern (inset in Fig. 2a), lattice fringes of 0.350 nm was observed in MoO_3 , representing the (040) planes [19]. Notably, the observed lattice fringe of the Na_xMoO_3 -3 (040) plane is 0.355 nm (larger than pure MoO_3), suggesting the structural distortion in the lattice (Fig. 2c). This is consistent with the XRD results. The energy-dispersive spectroscopy (EDS) mapping shows homogeneous distribution of Mo, O, and Na in Na_xMoO_3 (Figure S6). From the high-angle annular dark-field scanning transmission microscopy (HAADF-STEM) image in Figure S7, there are several light metal atoms in the van der Waals interlayers. We confirmed atoms' signals by line scanning at the chosen areas (Figure S8) [32,33]. Based on the size, it could be Na. To further ensure the composition and specific content, all samples' elemental content was analyzed. Excluding the Na ions in the background, we further confirmed the Na/Mo atomic ratio of different Na_xMoO_3 samples by ICP-MS (Table S3). The above results confirm the Na intercalation.

3.2. Electrochemical nitrogen reduction reaction performance

The electrochemical NRR performances of all the catalysts loaded on carbon fiber paper (CFP) are assessed in a H-type electrochemical cell filled with N_2 -saturated electrolyte under ambient conditions. Before testing, high-purity N_2 gas was sequentially passed through the absorbent bottles filled with acid and base to remove possible NH_3 and NO_x species, and then supplied continuously to the cathode chamber at a flow rate of $10 \text{ cm}^3/\text{min}$. We employ the as-prepared catalysts as the working electrode for NRR and use Ag/AgCl as the reference electrode. First, the NRR activity of the catalysts was determined through a series of blank experiments. Figure S9 exhibits the linear sweep voltammogram (LSV) curves of the Na_xMoO_3 -3 catalyst in Ar-saturated and N_2 -saturated electrolytes at the same potential range. The latter performed a higher current density, indicating considerable NRR activity. With the spectrophotometric indophenol blue method employed, we quantified the NRR performance of all samples. Fig. 3a shows the UV-Vis absorption spectra of the electrolytes before the test, after a one-hour test at an open circuit, using bare CFP, and at an N_2 -saturated/Ar-saturated atmosphere. The electrolyte shows much higher absorption after electrolysis under the N_2 -saturated atmosphere than under the other

conditions. It further proves the eNRR activity of the as-prepared catalyst. All the samples were tested at different potentials from -1.0 to -1.4 V , and the corresponding UV-vis absorption spectra are shown in Figure S10. We quantified the NH_3 yield rate and NH_3 FE (Fig. 3b and c) by the standard calibration curves (Figure S11). After Na intercalation, the NRR activity of the catalysts was first significantly improved and then decreased. Na_xMoO_3 -3 performs the best NH_3 yield of $41.3 \mu\text{g h}^{-1} \text{ mg}^{-1}$ and a FE of 21.4 % at -1.2 V . All samples' NRR activity was normalized by Mo content to calculate the TOF value (Table S4) [34,35]. And Na_xMoO_3 -3 has the best Intrinsic catalytic activity. Because Mo^{5+} sites provide most of NH_3 , the activity was also normalized by Mo^{5+} (determined by XPS), which is shown in Table S5. And Mo^{5+} sites have high activity. The NRR performances of Na_xMoO_3 -3 are superior to the many reported eNRR catalysts, and the detailed information is summarized in Fig. 3d and Table S6. Moreover, the possible by-products of N_2H_4 were tested by the Watt and Chrisp method, and the standard calibration curves are displayed in Figure S12a, b. We characterized the electrolyte after a one-hour test. As shown is Figure S12c, there is no N_2H_4 was detected in the liquid products, suggesting good NH_3 selectivity.

To further explore the contributing factors of NRR activity, a series of electrochemical properties were characterized. All samples' electrochemically active surface areas (ECSA) were assessed by cyclic voltammetry (CV) curves at different scan rates from 10 to 50 mV s^{-1} (Figure S13). We obtained the double layer capacitance (Cdl) values of different samples by linear fitting method (Figure S14). The ECSA is calculated from the equation ($\text{ECSA} = \text{Cdl}/\text{Cs}$) [36]. Cs is the specific capacitance of 0.04 mF cm^{-2} [37]. The final results are listed in Table S7. Compared to the pristine MoO_3 , Na_xMoO_3 performs larger Cdl. From the LSV results (Figure S15), with the Na content increasing, the current increased. According to the electrochemical impedance spectroscopy (EIS, Figure S16), the interaction between Na and MoO_3 reduces the charge-transfer resistance (Rct) of the catalysts. This phenomenon is consistent with the conclusion drawn from the LSV test, demonstrating that Na insertion modifies the intrinsic activity. However, better electrochemical performance would also facilitate the competing reaction of HER, resulting in a low FE. This may account for NRR activity reduction at high Na concentrations. Except for the intrinsic activity of the catalyst, the reaction conditions also determine the efficiency. To further modify the electrocatalytic condition, we tested the NRR activity of Na_xMoO_3 -3 at different electrolyte concentrations (Figure S17). The increase in the electrolyte concentration

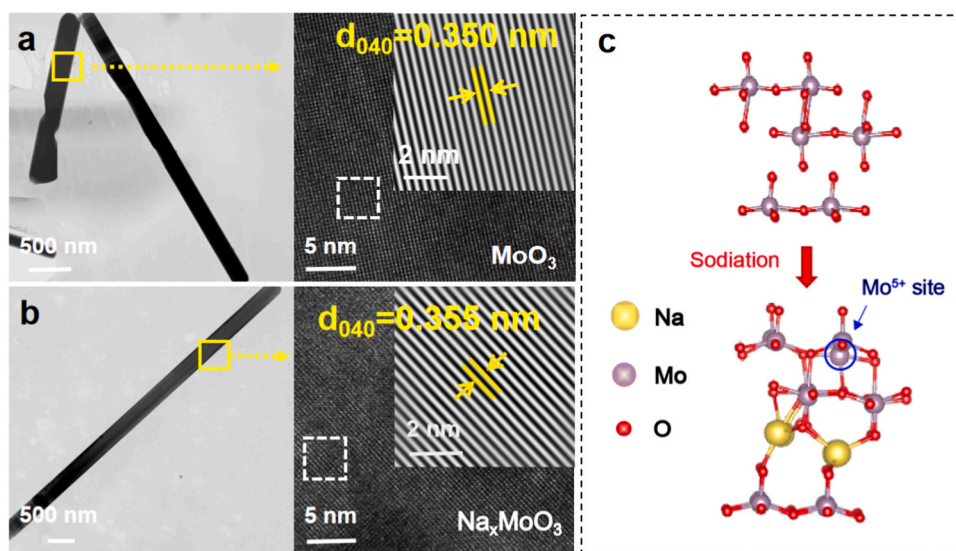


Fig. 2. TEM images and corresponding high-resolution TEM images (inset, the selected area electron diffraction pattern) of (a) MoO_3 and (b) Na_xMoO_3 -3. (c) MoO_3 octahedron after sodiation.

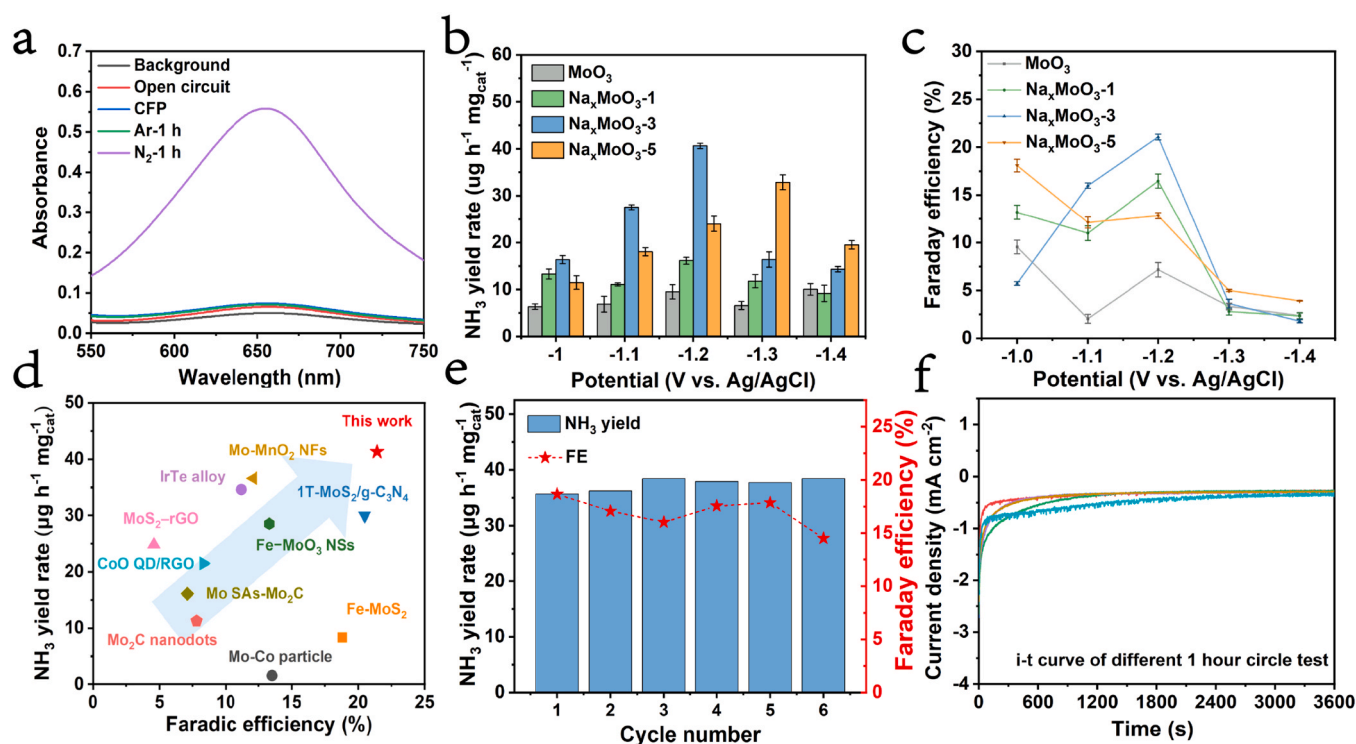


Fig. 3. (a) UV-Vis absorption spectra of electrolyte stained with indophenol indicator before NRR test, after 1 h electrolysis at open circuit potential, using bare carbon fiber paper and at N_2 /Ar-saturated atmosphere; (b) NH_3 yield rate and (c) NH_3 FE at different potentials on MoO_3 , Na_xMoO_3 -1, Na_xMoO_3 -3 and Na_xMoO_3 -5. (d) NRR activity comparison chart of Na_xMoO_3 -3. (e) Cycling tests of Na_xMoO_3 -3 at -1.2 V. (f) The chronoamperometry assessment of Na_xMoO_3 -3 electrolyzed at -1.2 V for 6 cycles.

improved the current density (Figure S18), and the best NRR performance was achieved with 0.5 M LiCl added to the electrolyte. The catalyst's stability is important for long-term use. After determining the optimal NRR conditions, we tested the stability of Na_xMoO_3 -3 for six one-hour cycles with no significant decrease in either NH_3 yield or FE (Figs. S19 and 3e). We tested the pH of the electrolyte and found that it remained weakly basic during the six-hour reaction, which ensures a relatively stable chemical environment (Figure S20). Also, the stable cycling current density is evidence of good stability (Fig. 3f). Continuing to prolong the reaction time to 24 h, the current did not decrease significantly (Figure S21), which ensures a continuous reaction. To determine the stability, we characterized the structure and morphology of the catalyst after electrochemical testing. From the XRD results, the structure of the catalyst remains virtually unchanged (Figure S22). According to the SEM and TEM images (Figure S23a and b), we can find that, due to the low working current density, the morphology of the catalyst has no significant change, which confirms the stability.

To further verify the contribution of intercalation, Na ions were removed by ion exchange [38]. We dispersed the Na_xMoO_3 -3 sample in 0.1 M HCl solution and stirred it overnight. After processing, the sample changed from dark blue to light blue (Figure S24b), which implies a decrease in Mo^{5+} content. We quantified the Na content of the acid-treated sample by ICP (Figure S24b). According to the results, almost no Na^+ is remaining, suggesting the successful removal of the cation. After the acid was treated, the NRR activity of the sample was reduced to nearly the same as that of pristine MoO_3 (Figure S24a, b). This is evidence that the Na intercalation influenced NRR activity by inducing Mo^{5+} sites. To exclude the effect of anions, we use different Na sources (NaCl) to prepare Na_xMoO_3 with different Na content by regulating the reactant concentration, and the color gradually deepened. This indicates the successful induction of Mo^{5+} . Then we test the NRR activity of them (Figure S25). The activity of these catalysts firstly increases and then decreases with improving Na content, which is in good

agreement with the experiment results above. It further proves the NRR activity derived from the cation effect. We infer that cations with different electron-donating capacities can produce different degrees of interaction between MoO_3 layers. To further verify the role of Na ions, other alkali metal ions with different electronegativity ($\text{Li}=1.0$, $\text{Na}=0.93$, $\text{K}=0.82$) were employed to prepare the samples (Li_xMoO_3 and K_xMoO_3) and the NRR performance were characterized under different potential (Figure S26). Among all the samples, the Na_xMoO_3 shows the best NH_3 yield rate, suggesting the optimal reducing effect of Na ions on MoO_3 . The results above illustrate that the cation effect is the key factor for NRR activity. Therefore, the stability of the catalysts is very important. We characterized the electrolyte after NRR testing by ICP (Table S8), and the Na content of the electrolyte was not increased. This indicates that Na is stable in the interlayer of the catalyst during the testing.

3.3. The reaction mechanism

DFT calculations were conducted to clarify the NRR mechanism of Na_xMoO_3 . We also apply DFT to pristine MoO_3 for comparison. Firstly, we have studied the Bader charges of Mo sites in MoO_3 (010) and Na_xMoO_3 (010) exposed surfaces (Figure S27 and S28). In contrast, more electrons migrate to the Mo sites after the Na intercalation [39]. Due to the electron donation effect, when Na enters into the interlayer of MoO_3 , it will interact with surface atoms and regulate the electron structure of Mo sites [40]. Thus, the Mo^{5+} sites with unsaturated oxygen coordination appear, which is consistent with the above XPS results. This may serve as the potential adsorption sites for N_2 . To further confirm the effect on the NRR activity, we simulated the adsorption and hydrogenation processes on MoO_3 and Na_xMoO_3 respectively. As shown in Fig. 4a, the differential charge density of $^*\text{N}_2$ on the Mo sites of Na_xMoO_3 and MoO_3 exhibits the adsorption states. Firstly, the yellow area on the Mo atoms in Na_xMoO_3 refers to the electron accumulation, indicating

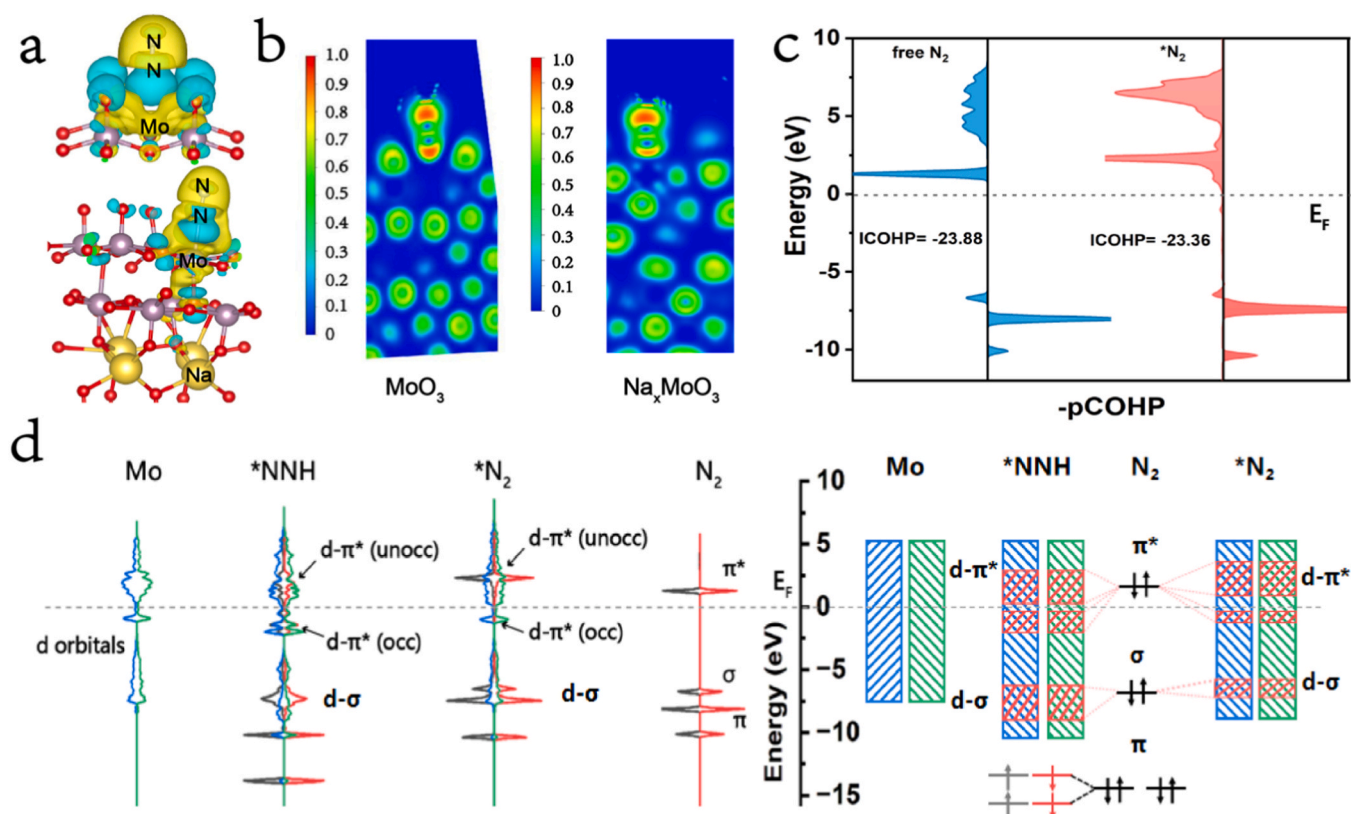


Fig. 4. (a) Charge density differences (yellow area is charge accumulation, blue area is charge depletion; purple sphere: Mo atom, red sphere: O atom, yellow sphere: Na atom and blue sphere: N atom) of adsorbed N_2 on MoO_3 (010) and Na_xMoO_3 (010) crystal plane. (b) Electronic location function (ELF) of MoO_3 (010) and Na_xMoO_3 (010) crystal plane. (c) Projected crystal orbital Hamilton populations (pCOHP) of free N_2 and adsorbed N_2 on Na_xMoO_3 . (d) Projected electronic density of states (pDOS) and schematic patterns of the interaction between the d orbitals of Mo in Na_xMoO_3 and the 2p orbitals of N_2 .

the lone pair electrons of N_2 entered the empty d orbital of Mo. This is a signal of successful adsorption. It also shows a charge accumulation between two N atoms in N_2^* , implying that d electrons of Mo transferred to the π^* orbitals of N_2 [41]. However, as a contrast, the pristine MoO_3 with saturated coordination possesses a much weaker adsorption of N_2 . We get a conclusion in N_2 temperature-programmed desorption (N_2 -TPD) that accords with the DFT results. Compared to pristine MoO_3 , Na_xMoO_3 has a stronger response to N_2 (Figure S29). There is a physics desorption temperature (150 °C) and a chemical desorption temperature (550 °C) for Na_xMoO_3 , confirming the better N_2 adsorption property [42,43]. The electron location function (ELF) of adsorbed N_2 on the Na_xMoO_3 (010) plane exhibits that the negative charge area is mainly forming on the adsorbed N_2 (Fig. 4b). Compared with the ELF result of pristine MoO_3 (010) (Fig. 4b), the activation of N_2 on Na_xMoO_3 is more efficient, which may be attributed to the changed electronic environment of the adsorption sites [44]. This suggests that Mo^{5+} sites interact with N_2 , and Mo's d orbital electrons can migrate rapidly to π^* orbitals of N_2 . Thus, the N-N bond of the adsorbed N_2 on Na_xMoO_3 is more active and prone to break. The integrated-crystal orbital Hamilton population (ICOHP) analysis was conducted to put deep insights into the d- π^* interaction. The more positive value for the computed ICOHPs of the adsorbed N_2 on Na_xMoO_3 (-23.36 eV) was obtained than of free N_2 (-23.88 eV) which suggests a stronger d- π^* interaction (Fig. 4c) [45,46]. It demonstrates the successful activation. As seen in Fig. 4d and S30, the energy levels of Mo in the Na_xMoO_3 (010) d orbitals match better with the π^* orbital of N_2 . Compared to that of MoO_3 , Na_xMoO_3 is more easily to adsorb N_2 to form a partial occupied of d- π^* interaction [47]. After bonding with a proton, the orbital energy level further decreases. Thus, more electrons occupied the d- π^* orbitals and N_2 was activated effectively [48]. The stronger interaction between the active sites of catalysts and nitrogen is also conducive to inhibiting competitive reactions. To

further explore it, Gibbs free energy of HER on the catalysts' surface was calculated [49]. As shown in Figure S31, H binds with Na_xMoO_3 weakly (0.51 eV), which is not conducive to H_2 production. The energy barrier to generate H_2 on Na_xMoO_3 is much higher than that of MoO_3 (0.34 eV), suggesting that the competitive reaction has less effect on Na_xMoO_3 . Above all, regulating the coordination structure to induce Mo^{5+} sites by Na intercalation can adjust the orbital energy level to match the N_2 orbital better. It's more conducive to adsorb and activate N_2 for Na_xMoO_3 .

To analyze the NRR process on Na_xMoO_3 , a time-resolved FT-IR Spectrometer is performed. As shown in Fig. 5a, the peaks of the products ($\text{NH}_3/\text{NH}_4^+$) are found at 1330/1440 cm^{-1} and gradually enhanced with the increase of reaction time from 0 to 120 s, confirming the production of NH_3 during NRR process [50]. Also, the peaks of -N-N stretching, - NH_2 wagging, and -N=N for N_2H_y intermediate species are also detected at 1080, 1150, and 2090 cm^{-1} respectively, indicating the NRR occurred [19]. To further reveal the mechanism of the NRR process on catalyst surface, free energy was calculated for NRR process on Mo sites of pristine MoO_3 (010) and Na_xMoO_3 (010) exposed surfaces respectively. As shown in Figure S32, the interaction between N_2 molecular and MoO_3 (010) surface is very weak, which is not favorable for adsorbing and activating N_2 . After inducing Mo^{5+} sites, Gibbs free energy of the adsorption step and the first hydrogenation process ($\text{H}^+ + \text{e}^- + \text{N}_2 \rightarrow \text{NNH}^*$) of NRR is significantly reduced, indicating that the reaction tended to be spontaneous. The adsorption energy of N_2 (Eadsorption) is calculated based on the theoretical formula (Eadsorption = $E_{\text{total}} - (E(010) + E_{\text{nitrogen}})$) [51]. $E(010)$ is the total energy of the (010) plane of MoO_3 and Na_xMoO_3 , and E_{nitrogen} is the total energy of N_2 . And the obtained adsorption energy (Eadsorption) of N_2 on the MoO_3 (010) surface and Na_xMoO_3 (010) surface is -0.154 and -0.366 eV respectively (Table S9), further showing the accelerated NRR process on Na_xMoO_3 . Previous calculation results suggest that the

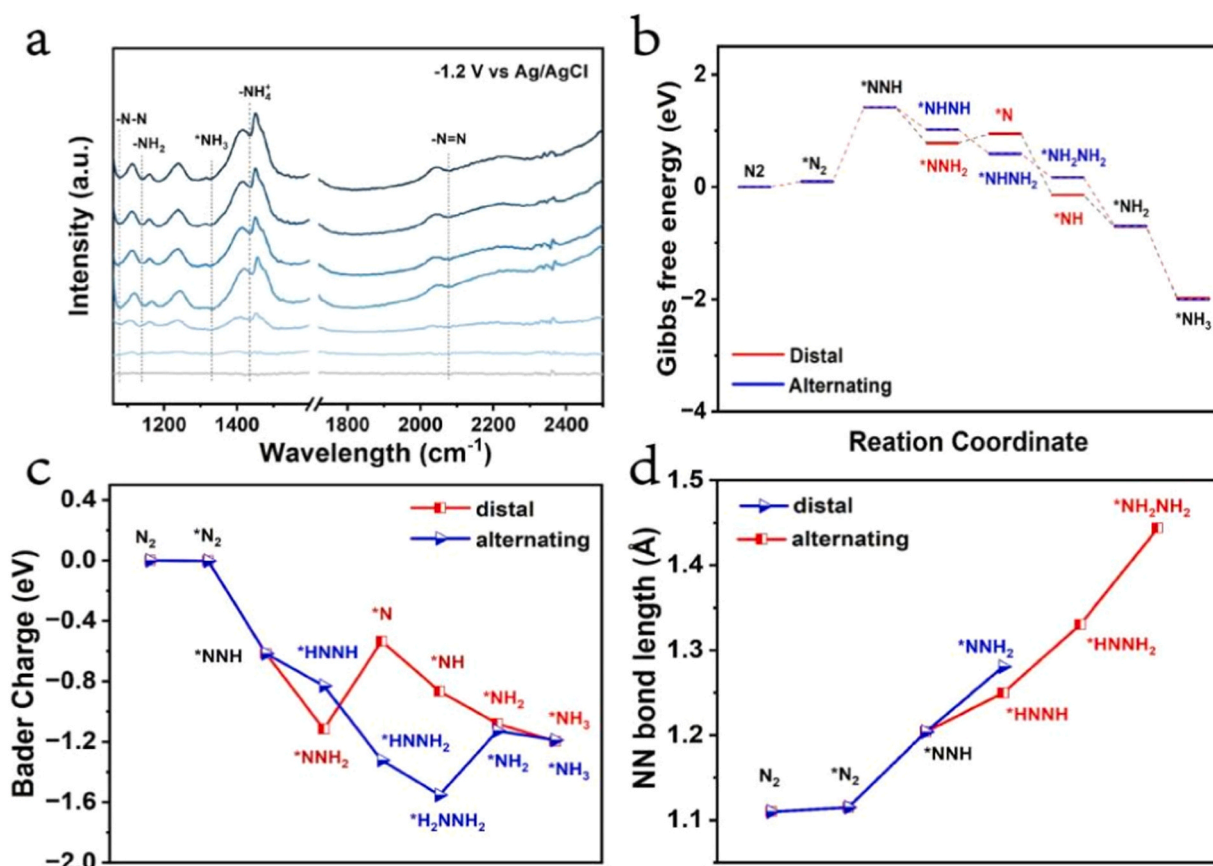


Fig. 5. (a) FTIR spectra at -1.2 V versus Ag/AgCl for Na_xMoO_3 using N_2 as the feeding gas. (b) Gibbs free energy for NRR process on Na_xMoO_3 . (c) The change of bader charge during NRR process on the Na_xMoO_3 (010) crystal plane. (d) The change of N-N bond length during the NRR process on the Na_xMoO_3 (010) crystal plane.

dropped orbitals energy level of Mo sites in Na_xMoO_3 can strengthen the N_2 adsorption and donate electrons to π^* orbitals of N_2 , thus breaking the N-N bond and accelerating the N_2 activation. After that, the N_2 will be further activated taking the distal (Figure S33) and alternating pathway (Figure S34). Gibbs free energy was applied for further discussing the spontaneity of the NRR process (Fig. 5b), while detailed information about the intermediates is shown in Tables S10 and S11. As shown in Fig. 5b, Gibbs free energy of the alternating pathway goes downhill, indicating the spontaneity of subsequent reactions. To explore the NRR pathway, the Bader charges in distal and alternating reaction pathways were simulated (Fig. 5c). There is a similar decrease trend in the Bader charges of the adsorption step and the former two hydrogenation step of the alternating pathway and distal pathway. When the hydrogenation steps further occur, the Bader charges of *NHNH_2 in alternating pathway is $1.32 |e|$. Compared to the distal pathway (*N : $0.53 |e|$), there is more electrons transfer from Na_xMoO_3 to the produced immediate along alternating pathway, indicating a more efficient activation of N_2 [29]. Furthermore, we calculated the N-N bond length during reaction to reveal the activation process. As shown in Fig. 5d, along the distal mechanism, the N-N bond is extended from 1.11 \AA (N_2) to 1.28 \AA (*NNH_2). However, for the alternating mechanism, the N-N bond is eventually lengthened to 1.44 \AA ($\text{*NH}_2\text{NH}_2$), implying more sufficient dissociation of N_2 [38]. Thus, the above results all suggest that the NRR on the Na_xMoO_3 (010) surface prefers to take the alternating reaction pathway.

4. Conclusions

In summary, an intercalation method was adopted to regulate the coordination structure of MoO_3 and successfully induced the Mo^{5+}

active sites. With the construction of Mo^{5+} sites, the as-prepared Na_xMoO_3 owns better N_2 adsorption performance, which is theoretically and experimentally confirmed. DFT calculation reveals that introducing Mo^{5+} sites in the Na_xMoO_3 regulates the orbital energy level to make it well-matched with the π^* orbitals of N_2 , thus leading to efficient activation. Electrochemical measurements showed that the optimized Na_xMoO_3 presented a rapid NH_3 yield of $41.3 \mu\text{g h}^{-1} \text{ mg}^{-1}$ and an FE of 21.4 %, which is a nearly five-fold improvement than that of pristine MoO_3 , outperforming lots of recent reported eNRR catalysts. This study presents theoretical and experimental guidance for developing efficient Mo-based eNRR catalysts.

CRediT authorship contribution statement

Aofei Xu: Formal analysis. **Guidong Yang:** Writing – review & editing. **Jia Li:** Formal analysis. **Yuxi Ren:** Writing – original draft. **Jiantao Liu:** Formal analysis. **Ben Chong:** Formal analysis. **Hang Xiao:** Formal analysis. **Mengyang Xia:** Supervision. **Zhiwei Ren:** Formal analysis. **Honghui Ou:** Writing – review & editing. **Song Kou:** Formal analysis.

Declaration of Competing Interest

The authors declare no conflict of interest.

Data Availability

No data was used for the research described in the article.

Acknowledgements

This work is supported by the National Key R&D Program of China (2020YFA0710000), National Natural Science Foundation of China (Grant No. U22A20391, 22078256, 22302154), Innovation Capability Support Program of Shaanxi (NO. 2023-CX-TD-26), the Programme of Introducing Talents of Discipline to Universities (B23025), and the Shaanxi Provincial Key Research and Development Program (2021SF-176).

Appendix A. Supporting information

Supplementary data associated with this article can be found in the online version at [doi:10.1016/j.apcatb.2024.124066](https://doi.org/10.1016/j.apcatb.2024.124066).

References

- [1] F. Xu, F. Wu, K. Zhu, Z. Fang, D. Jia, Y. Wang, G. Jia, J. Low, W. Ye, Z. Sun, P. Gao, Y. Xiong, Boron doping and high curvature in Bi nanorolls for promoting photoelectrochemical nitrogen fixation, *Appl. Catal. B: Environ.* 284 (2021) 119689, <https://doi.org/10.1016/j.apcatb.2020.119689>.
- [2] X. Xue, R. Chen, C. Yan, P. Zhao, Y. Hu, W. Zhang, S. Yang, Z. Jin, Review on photocatalytic and electrocatalytic artificial nitrogen fixation for ammonia synthesis at mild conditions: advances, challenges and perspectives, *Nano Res.* 12 (2019) 1229–1249, <https://doi.org/10.1007/s12274-018-2268-5>.
- [3] X. Hu, Y. Sun, S. Guo, J. Sun, Y. Fu, S. Chen, S. Zhang, J. Zhu, Identifying electrocatalytic activity and mechanism of $\text{Ce}_{1/3}\text{NbO}_3$ perovskite for nitrogen reduction to ammonia at ambient conditions, *Appl. Catal. B: Environ.* 280 (2021) 119419, <https://doi.org/10.1016/j.apcatb.2020.119419>.
- [4] D.K. Yesudoss, H. Chun, B. Han, S. Shanmugam, Accelerated N_2 reduction kinetics in hybrid interfaces of NbTiO_4 and nitrogen-doped carbon nanorod via synergistic electronic coupling effect, *Appl. Catal. B: Environ.* 304 (2022) 120938, <https://doi.org/10.1016/j.apcatb.2021.120938>.
- [5] B. Yan, Y. Li, W. Cao, Z. Zeng, P. Liu, Z. Ke, G. Yang, Highly efficient and highly selective CO_2 reduction to CO driven by laser, *Joule* 6 (2022) 2735–2744, <https://doi.org/10.1016/j.joule.2022.11.005>.
- [6] T. Wu, B. Chang, Y. Li, X. Zhang, X. Zhao, Z. Liu, G. Zhang, X. Liu, L. Zhao, Y. Zhang, H. Zhang, H. Liu, W. Zhou, Laser-induced plasma and local temperature field for high-efficiency ammonia synthesis, *Nano Energy* 116 (2023) 108855, <https://doi.org/10.1016/j.nanoen.2023.108855>.
- [7] L. Li, C. Tang, X. Cui, Y. Zheng, X. Wang, H. Xu, S. Zhang, T. Shao, K. Davey, S. Qiao, Efficient nitrogen fixation to ammonia through integration of plasma oxidation with electrocatalytic reduction, *Angew. Chem. Int. Ed.* 60 (2021) 14131–14137, <https://doi.org/10.1002/anie.202104394>.
- [8] L. Li, W. Yu, W. Gong, H. Wang, C.-L. Chiang, Y. Lin, J. Zhao, L. Zhang, J.-M. Lee, G. Zou, Sulfur-induced electron redistribution of single molybdenum atoms promotes nitrogen electroreduction to ammonia, *Appl. Catal. B: Environ.* 321 (2023) 122038, <https://doi.org/10.1016/j.apcatb.2022.122038>.
- [9] R. Liu, H. Fei, J. Wang, T. Guo, F. Liu, J. Wang, Z. Wu, D. Wang, Insights of active sites separation mechanism for highly efficient electrocatalytic N_2 reduction to ammonia over glucose-induced metallic MoS_2 , *Appl. Catal. B: Environ.* 337 (2023) 122997, <https://doi.org/10.1016/j.apcatb.2023.122997>.
- [10] B.M. Hoffman, D. Lukoyanov, Z.-Y. Yang, D.R. Dean, L.C. Seefeldt, Mechanism of nitrogen fixation by nitrogenase: The next stage, *Chem. Rev.* 114 (2014) 4041–4062, <https://doi.org/10.1021/cr400641x>.
- [11] B.M. Hoffman, D. Lukoyanov, D.R. Dean, L.C. Seefeldt, Nitrogenase: a draft mechanism, *Acc. Chem. Res.* 46 (2013) 587–595, <https://doi.org/10.1021/ar300267m>.
- [12] R. Liu, H. Fei, J. Wang, T. Guo, F. Liu, Z. Wu, D. Wang, Unveiling the synergistic effect between the metallic phase and bridging S species over MoS_2 for highly efficient nitrogen fixation, *Appl. Catal. B: Environ.* 343 (2024) 123469, <https://doi.org/10.1016/j.apcatb.2023.123469>.
- [13] D. Yang, T. Chen, Z. Wang, Electrochemical reduction of aqueous nitrogen (N_2) at a low overpotential on (110)-oriented Mo nanofilm, *J. Mater. Chem. A* 5 (2017) 18967–18971, <https://doi.org/10.1039/C7TA06139K>.
- [14] H. Cheng, L.-X. Ding, G.-F. Chen, L. Zhang, J. Xue, H. Wang, Molybdenum carbide nanodots enable efficient electrocatalytic nitrogen fixation under ambient conditions, *Adv. Mater.* 30 (2018) 1803694, <https://doi.org/10.1002/adma.201803694>.
- [15] H.Y. Zhou, Y.B. Qu, Y.C. Fan, Z.L. Wang, X.Y. Lang, J.C. Li, Q. Jiang, Multi-site intermetallic Ni_3Mo effectively boosts selective ammonia synthesis, *Appl. Catal. B: Environ.* 339 (2023) 123133, <https://doi.org/10.1016/j.apcatb.2023.123133>.
- [16] J. Wang, Z. Jiang, G. Peng, E. Hoenig, G. Yan, M. Wang, Y. Liu, X. Du, C. Liu, Surface valence state effect of MoO_{2+x} on electrochemical nitrogen reduction, *Adv. Sci.* 9 (2022) 2104857, <https://doi.org/10.1002/advsc.202104857>.
- [17] Z. Yan, J. Fan, Z. Zuo, Z. Li, J. Zhang, NH_3 adsorption on the Lewis and Brønsted acid sites of MoO_3 (010) surface: a cluster DFT study, *Appl. Surf. Sci.* 288 (2014) 690–694, <https://doi.org/10.1016/j.apsusc.2013.10.105>.
- [18] H. Tan, Q. Ji, C. Wang, H. Duan, Y. Kong, Y. Wang, S. Feng, L. Lv, F. Hu, W. Zhang, W. Chu, Z. Sun, W. Yan, Asymmetrical π back-donation of hetero-dicationic Mo^{4+} - Mo^{6+} pairs for enhanced electrochemical nitrogen reduction, *Nano Res.* 15 (2022) 3010–3016, <https://doi.org/10.1007/s12274-021-3934-6>.
- [19] Q. Liu, T. Xu, Y. Luo, Q. Kong, T. Li, S. Lu, A.A. Alshehri, K.A. Alzahrani, X. Sun, Recent advances in strategies for highly selective electrocatalytic N_2 reduction toward ambient NH_3 synthesis, *Curr. Opin. Electrochem.* 29 (2021) 100766, <https://doi.org/10.1016/j.coelec.2021.100766>.
- [20] W. Liu, C. Li, Q. Xu, P. Yan, C. Niu, Y. Shen, P. Yuan, Y. Jia, Anderson Localization in 2D amorphous MoO_{3-x} monolayers for electrochemical ammonia synthesis, *ChemCatChem* 11 (2019) 5412–5416, <https://doi.org/10.1002/cctc.201901171>.
- [21] H. Xian, H. Guo, J. Xia, Q. Chen, Y. Luo, R. Song, T. Li, E. Traversa, Iron-doped MoO_3 nanosheets for boosting nitrogen fixation to ammonia at ambient conditions, *ACS Appl. Mater. Interfaces* 13 (2021) 7142–7151, <https://doi.org/10.1021/acsami.0c19644>.
- [22] W. Huang, K. Zhang, B. Yuan, L. Yang, M. Zhu, Predominant intercalation of H^+ enables ultrahigh rate capability of oxygen deficient MoO_3 for aqueous Al-ion batteries, *Energy Storage Mater.* 50 (2022) 152–160, <https://doi.org/10.1016/j.ensm.2022.05.016>.
- [23] W. Yang, J. Xiao, Y. Ma, S. Cui, P. Zhang, P. Zhai, L. Meng, X. Wang, Y. Wei, Z. Du, B. Li, Z. Sun, S. Yang, Q. Zhang, Y. Gong, Tin intercalated ultrathin MoO_3 nanoribbons for advanced lithium-sulfur batteries, *Adv. Energy Mater.* 9 (2019) 1803137, <https://doi.org/10.1002/aenm.201803137>.
- [24] M. Wang, K.J. Koski, Reversible chemochromic MoO_3 nanoribbons through zerovalent metal intercalation, *ACS Nano* 9 (2015) 3226–3233, <https://doi.org/10.1021/acs.nano.5b00336>.
- [25] H. Yin, Z. Chen, Y. Peng, S. Xiong, Y. Li, H. Yamashita, J. Li, Dual active centers bridged by oxygen vacancies of ruthenium single-atom hybrids supported on molybdenum oxide for photocatalytic ammonia synthesis, *Angew. Chem. Int. Ed.* 61 (2022), <https://doi.org/10.1002/anie.202114242>.
- [26] N. Zheng, G. Jiang, X. Chen, J. Mao, Y. Zhou, Y. Li, Rational design of a tubular, interlayer expanded MoS_2 -N/O doped carbon composite for excellent potassium-ion storage, *J. Mater. Chem. A* 7 (2019) 9305–9315, <https://doi.org/10.1039/C9TA00423H>.
- [27] Y. Wang, Q. Pan, Y. Qiao, X. Wang, D. Deng, F. Zheng, B. Chen, J. Qiu, Layered metal oxide nanosheets with enhanced interlayer space for electrochemical deionization, *Adv. Mater.* (2023) 2210871, <https://doi.org/10.1002/adma.202210871>.
- [28] H. Ou, Y. Qian, L. Yuan, H. Li, L. Zhang, S. Chen, M. Zhou, G. Yang, D. Wang, Y. Wang, Spatial position regulation of Cu single atom site realizes efficient nanozyme photocatalytic bactericidal activity, *Adv. Mater.* 35 (2023) 2305077, <https://doi.org/10.1002/adma.202305077>.
- [29] M. Sun, G. Wu, J. Jiang, Y. Yang, A. Du, L. Dai, X. Mao, Q. Qin, Carbon-anchored molybdenum oxide nanoclusters as efficient catalysts for the electrosynthesis of ammonia and urea, *Angew. Chem. Int. Ed.* 62 (2023) e202301957, <https://doi.org/10.1002/anie.202301957>.
- [30] Z. Zhou, Y. Wang, F. Peng, F. Meng, J. Zha, L. Ma, Y. Du, N. Peng, L. Ma, Q. Zhang, L. Gu, W. Yin, Z. Gu, C. Tan, Intercalation-activated layered MoO_3 nanobelts as biodegradable nanozymes for tumor-specific photo-enhanced catalytic therapy, *Angew. Chem. Int. Ed.* 61 (2022), <https://doi.org/10.1002/anie.202115939>.
- [31] H. Ren, L. Zhang, J. Zhang, T. Miao, R. Yuan, W. Chen, Z. Wang, J. Yang, B. Zhao, Na^+ pre-intercalated $\text{Na}_{0.11}\text{MnO}_2$ on three-dimensional graphene as cathode for aqueous zinc ion hybrid supercapacitor with high energy density, *Carbon* 198 (2022) 46–56, <https://doi.org/10.1016/j.carbon.2022.07.008>.
- [32] J. Liang, Z. Li, L. Zhang, X. He, Y. Luo, D. Zheng, Y. Wang, T. Li, H. Yan, B. Ying, S. Sun, Q. Liu, M.S. Hamdy, B. Tang, X. Sun, Advances in ammonia electrosynthesis from ambient nitrate/nitrite reduction, *Chem* 9 (2023) 1768–1827, <https://doi.org/10.1016/j.chempr.2023.05.037>.
- [33] H. Zhao, J. Xiang, Z. Sun, S. Shang, K. Chu, Electroreduction of nitrite to ammonia over a cobalt single-atom catalyst, *ACS Sustain. Chem. Eng.* 12 (2024) 2783–2789, <https://doi.org/10.1021/acssuschemeng.3c07388>.
- [34] M.A. Mushtaq, A. Kumar, W. Liu, Q. Ji, Y. Deng, G. Yasin, A. Saad, W. Raza, J. Zhao, S. Ajmal, Y. Wu, M. Ahmad, N.U.R. Lashari, Y. Wang, T. Li, S. Sun, D. Zheng, Y. Luo, X. Cai, X. Sun, A metal coordination number determined catalytic performance in manganese borides for ambient electrolysis of nitrogen to ammonia, *Adv. Mater.* (2024) 2313086, <https://doi.org/10.1002/adma.202313086>.
- [35] H. Ou, G. Li, W. Ren, B. Pan, G. Luo, Z. Hu, D. Wang, Y. Li, Atomically dispersed Au-ssisted C–C coupling on red phosphorus for CO_2 photoreduction to C_2H_6 , *J. Am. Chem. Soc.* 144 (2022) 22075–22082, <https://doi.org/10.1021/jacs.2c09424>.
- [36] H. Chen, Z. Xu, S. Sun, Y. Luo, Q. Liu, M.S. Hamdy, Z. Feng, X. Sun, Y. Wang, Plasma-etched Ti_2O_3 with oxygen vacancies for enhanced NH_3 electrosynthesis and Zn-N_2 batteries, *Inorg. Chem. Front.* 9 (2022) 4608–4613, <https://doi.org/10.1039/D2QI01173E>.
- [37] H. Chen, J. Liang, K. Dong, L. Yue, T. Li, Y. Luo, Z. Feng, N. Li, M.S. Hamdy, A. A. Alshehri, Y. Wang, X. Sun, Q. Liu, Ambient electrochemical N_2 -to- NH_3 conversion catalyzed by TiO_2 decorated *Juncus effusus*-derived carbon microtubes, *Inorg. Chem. Front.* 9 (2022) 1514–1519, <https://doi.org/10.1039/D2QI00140C>.
- [38] Y. Luo, Q. Pan, H. Wei, Y. Huang, L. Tang, Z. Wang, C. Yan, J. Mao, K. Dai, Q. Wu, X. Zhang, J. Zheng, Fundamentals of ion-exchange synthesis and its implications in layered oxide cathodes: recent advances and perspective, *Adv. Energy Mater.* 13 (2023) 2300125, <https://doi.org/10.1002/aenm.202300125>.
- [39] M. Xia, B. Chong, X. Gong, H. Xiao, H. Li, H. Ou, B. Zhang, G. Yang, Ti^{2+} Site-promoted $\text{N}\equiv\text{N}$ bond activation in LaTiO_{3-x} nanosheets for nitrogen photofixation, *ACS Catal.* 13 (2023) 12350–12362, <https://doi.org/10.1021/acscatal.3c02198>.
- [40] Z. Tang, D. Wang, B. Chen, D. Huo, Y. Zhang, X. Wang, H. Tang, G. Meng, $\text{Na}_x\text{WO}_{3-x}$ nanosheet array via in situ Na intercalation for surface-enhanced Raman

- scattering detection of methylene blue, *ACS Appl. Nano Mater.* 5 (2022) 7841–7849, <https://doi.org/10.1021/acsanm.2c00862>.
- [41] X. Ren, M. Xia, B. Chong, X. Yan, B. Lin, G. Yang, Transition metal modified 3DOM WO_3 with activated $\text{N}\equiv\text{N}$ bond triggering high-efficiency nitrogen photoreduction, *Chem. Eng. Sci.* 257 (2022) 117734, <https://doi.org/10.1016/j.ces.2022.117734>.
- [42] K. Chu, Y. Liu, Y. Li, Y. Guo, Y. Tian, H. Zhang, Multi-functional Mo-doping in MnO_2 nanoflowers toward efficient and robust electrocatalytic nitrogen fixation, *Appl. Catal. B: Environ.* 264 (2020) 118525, <https://doi.org/10.1016/j.apcatb.2019.118525>.
- [43] X. Li, P. Shen, Y. Luo, Y. Li, Y. Guo, H. Zhang, K. Chu, PdFe single-atom alloy metallene for N_2 electroreduction, *Angew. Chem. Int. Ed.* 134 (2022) e202205923, <https://doi.org/10.1002/ange.202205923>.
- [44] B. Xu, H. Li, B. Chong, B. Lin, X. Yan, G. Yang, Zn vacancy-tailoring mediated ZnIn_2S_4 nanosheets with accelerated orderly charge flow for boosting photocatalytic hydrogen evolution, *Chem. Eng. Sci.* 270 (2023) 118533, <https://doi.org/10.1016/j.ces.2023.118533>.
- [45] H. Xiao, M. Xia, B. Chong, H. Li, B. Lin, G. Yang, D-band center modulation of B-mediated FeS_2 to activate molecular nitrogen for electrocatalytic ammonia synthesis, *Appl. Catal. B: Environ.* 343 (2024) 123474, <https://doi.org/10.1016/j.apcatb.2023.123474>.
- [46] K. Chen, J. Xiang, Y. Guo, X. Liu, X. Li, K. Chu, Pd_1Cu single-atom alloys for high-current-density and durable NO -to- NH_3 electroreduction, *Nano Lett.* 24 (2024) 541–548, <https://doi.org/10.1021/acs.nanolett.3c02259>.
- [47] J.-C. Liu, X.-L. Ma, Y. Li, Y.-G. Wang, H. Xiao, J. Li, Heterogeneous Fe_3 single-cluster catalyst for ammonia synthesis via an associative mechanism, *Nat. Commun.* 9 (2018) 1610, <https://doi.org/10.1038/s41467-018-03795-8>.
- [48] G. Zhou, T. Li, R. Huang, P. Wang, B. Hu, H. Li, L. Liu, Y. Sun, Recharged catalyst with memristive nitrogen reduction activity through learning networks of spiking neurons, *J. Am. Chem. Soc.* 143 (2021) 5378–5385, <https://doi.org/10.1021/jacs.0c12458>.
- [49] L. Ouyang, J. Liang, Y. Luo, D. Zheng, S. Sun, Q. Liu, M.S. Hamdy, X. Sun, B. Ying, Recent advances in electrocatalytic ammonia synthesis, *Chin. J. Catal.* 50 (2023) 6–44, [https://doi.org/10.1016/S1872-2067\(23\)64464-X](https://doi.org/10.1016/S1872-2067(23)64464-X).
- [50] Y. Ren, C. Yu, X. Han, X. Tan, Q. Wei, W. Li, Y. Han, L. Yang, J. Qiu, Methanol-mediated electrosynthesis of ammonia, *ACS Energy Lett.* 6 (2021) 3844–3850, <https://doi.org/10.1021/acseenergylett.1c01893>.
- [51] H. Li, M. Xia, B. Chong, H. Xiao, B. Zhang, B. Lin, B. Yang, G. Yang, Boosting photocatalytic nitrogen fixation via constructing low-oxidation-state active sites in the nanoconfined spinel iron cobalt oxide, *ACS Catal.* 12 (2022) 10361–10372, <https://doi.org/10.1021/acscatal.2c02282>.